

Lattice dynamics and ferroelectric properties of nitride perovskite LaWN₃

Yue-Wen Fang^{1,2,†}, Craig A.J. Fisher², Akihide Kuwabara², Xin-Wei Shen¹, Takafumi Ogawa², Hiroki Moriwake^{2,†}, Rong Huang^{1,2}, and Chun-Gang Duan^{1,3,*}

¹Key Laboratory of Polar Materials and Devices,
Ministry of Education,
Department of Electronic Engineering,
East China Normal University, Shanghai 200241, China
²Nanostructures Research Laboratory,
Japan Fine Ceramics Center, Nagoya 456-8587, Japan
³Collaborative Innovation Center of Extreme Optics,
Shanxi University, Taiyuan, Shanxi 030006, China

(Dated: May 2, 2023)

Using first-principles calculations we examine the crystal structures and phase transitions of nitride perovskite LaWN₃. Lattice dynamics calculations indicate that the ground-state structure belongs to space group *R3c*. Two competitive phase transition pathways are identified which are characterized by symmetry-adapted distortion modes. The results suggest that *R3c* LaWN₃ should be an excellent ferroelectric semiconductor: its large spontaneous polarization of around 61 $\mu\text{C}/\text{cm}^2$ is comparable to that of PbTiO₃, and its band gap is about 1.72 eV. Ferroelectricity is found to result from the *B*-site instability driven by hybridization between W-5*d* and N-2*p* orbitals. These properties make LaWN₃ an attractive candidate material for use in ferroelectric memory devices and photovoltaic cells.

I. INTRODUCTION

Perovskites *ABX*₃, in which 12-fold coordinated *A*-site cations each sit between eight corner-sharing *BX*₆ octahedra, exhibit a vast variety of physical, chemical, electrical and magnetic properties, making them of enormous interest from both a scientific and technological point of view.^{1–5} For example, ferroelectric oxide perovskites *ABO*₃, long established as tunable capacitors, ultrasound generators, infrared sensors, and fuel injectors, are now being developed for use in data storage devices^{6,7} and photovoltaic cells.^{8,9}

At present, commercial ferroelectric random-access memory uses lead zirconate titanate (PZT),¹⁰ which is potentially hazardous because of the toxicity of lead.¹¹ There is thus a strong incentive to develop alternative materials exhibiting excellent ferroelectric or photoferroic properties that are non-toxic and environmentally benign.

A number of studies in recent years have used computational screening methods to search for novel candidate ferroelectric materials.^{12–15} Of the many new systems identified, perovskites with the LiNbO₃-type structure that crystallize in space group *R3c* are particularly interesting because the driving mechanisms behind their ferroelectricity are very different to those in the extensively studied BaTiO₃ and PbTiO₃ systems.^{16–21} For example, LiNbO₃-type FeTiO₃ has been predicted to exhibit a spontaneous polarization, despite its lack of lone-pair electrons, that simultaneously induces a weak ferromagnetism whose direction can be controlled with an electric field.²² Benedek and Fennie showed that the ferroelectricity in FeTiO₃ is mostly attributable to displacement of *A*-site cations, with a minor contribution from off-center

B-site cations.²³ Varga *et al.* synthesized *R3c* FeTiO₃ at high pressure and confirmed the coexistence of weak ferromagnetism and ferroelectricity (multiferroicity) in this material.²⁴

More recently, Wang *et al.* predicted ZnFe_{0.5}Os_{0.5}O₃ to be a polar LiNbO₃-type perovskite with strong ferroelectricity ($\sim 54.7 \mu\text{C}/\text{cm}^2$) caused by *A*-site displacements, at the same time showing that the ferroelectric ordering may be strongly coupled with ferrimagnetism above room temperature.¹⁷ Ye and Vanderbilt also identified ZnFe_{0.5}Os_{0.5}O₃ and other LiNbO₃-type perovskites such as LiZr_{0.5}Te_{0.5}O₃ as ferroelectrics by calculating energy profiles of the ferroelectric reversal paths from first principles.¹³

As the above outline suggests, considerable progress has been made in our understanding of the ferroelectric behavior of LiNbO₃-type oxide perovskites. Relatively little attention has been paid, however, to LiNbO₃-type perovskites in which O is completely replaced with other 2nd row elements such as N or F.²⁵

Here we report on the ferroelectric behavior of nitride perovskite LaWN₃, which was recently identified as a stable semiconductor based on high-throughput first-principles calculations.^{26,27} These calculations predicted the ground state of LaWN₃ to have a LiNbO₃-type structure with *R3c* symmetry, which can be derived from the aristotype (cubic) perovskite structure by two different phase transition sequences, viz., $Pm\bar{3}m \rightarrow R\bar{3}c \rightarrow R3c$ and $Pm\bar{3}m \rightarrow R3m \rightarrow R3c$. The corresponding structural distortions associated with each phase transition can be interpreted in terms of symmetry-adapted modes. In this study we use first-principles calculations to show that *R3c* LaWN₃ exhibits robust ferroelectricity with a polarization of 61 $\mu\text{C}/\text{cm}^2$. Surprisingly, although the Gold-

schmidt tolerance factor, t , is less than 1, the ferroelectric instability is found to be driven by B -site atom displacement rather than A -site atom displacement, unlike the well-known ferroelectric LiNbO_3 -type semiconductor ZnSnO_3 ²⁸ and ferroelectric metal LiOsO_3 .^{29,30}

The rest of the paper is organized as follows: In Sec. II we provide details of the first-principles calculation methods. The results are presented and discussed in Sec. III, and conclusions are summarized in Sec. IV.

II. COMPUTATIONAL DETAILS

First-principles density functional theory (DFT) calculations are performed using the Vienna *ab initio* Simulation Package (VASP)^{31,32} based on the projector-augmented wave method and a plane wave basis set.³³ $5p^65d^16s^2$ for La, $5d^46s^2$ for W, and $2s^22p^3$ for N are explicitly included as valence electrons in the pseudopotentials. The local density approximation (LDA) is used for exchange-correlation terms. A planewave cutoff of 520 eV is used in all cases. $13 \times 13 \times 13$ and $7 \times 7 \times 7$ Monkhorst-Pack k -meshes³⁴ are used for unit cell and $2 \times 2 \times 2$ supercell calculations, respectively. All structures are fully relaxed until Hellmann-Feynman forces on each atom converge to below 10^{-3} eV·Å⁻¹.

Phonon calculations using $2 \times 2 \times 2$ supercells are carried out in which force constants are calculated based on density functional perturbation theory³⁵ as implemented in VASP. Phonon band structures and phonon densities of states at arbitrary q -vectors are computed using the code phonopy.³⁶ In addition, except for the phases of LaWN_3 showing metallic properties, longitudinal-optical-transverse-optical splitting is included using a non-analytical term correction.³⁷ Ferroelectric polarization is calculated using the Berry phase method.³⁸ The effects of hybridization of electronic states on ferroelectric properties are examined by the orbital selective external potential (OSEP) method.^{2,39}

Because of the well-known underestimation of the bandgap using standard DFT, in addition to LDA calculations we also use the hybrid exchange-correlation functional of Heyd, Scuseria, and Ernzerhof (HSE)⁴¹ in a few instances. In these cases, Brillouin zone sampling of the 10-atom unit cell is limited to a $5 \times 5 \times 5$ k -mesh grid.

III. RESULTS AND DISCUSSION

A. Lattice dynamics of the cubic phase

The Goldschmidt tolerance factor for perovskite compounds ABX_3 is defined as $t = \frac{R_A + R_X}{\sqrt{2}(R_B + R_X)}$, where R_A , R_B , and R_X are the radii of ions on A , B , and X sites, respectively. The tolerance factor gives an indication of the stability and amount of distortion of the structure^{42,43} relative to the cubic aristotype, for which $t = 1$. If $t \neq 1$, octahedral rotations or off-center displacements are

expected to occur to optimize the coordination environments of A -site and B -site atoms. In the case of LaWN_3 , the ionic radii of La and W in 12- and 6-fold coordination ($R_{\text{La}} = 1.36$ Å and $R_{\text{W}} = 0.6$ Å), respectively and the ionic radius of N ($R_{\text{N}} = 1.46$ Å for 4-fold coordination) give $t = 0.969$; the cubic form of LaWN_3 is thus not expected to be the ground-state structure, as the large deviation from $t = 1$ indicates distortions to low-symmetry structures should be more energetically favorable.

DFT calculations to assess the structural stability of cubic LaWN_3 (space group $Pm\bar{3}m$) were performed using the LDA functional. The unit cell of cubic LaWN_3 is illustrated in Fig. 1(a), and the Brillouin zone path used in phonon dispersion calculations is shown in Fig. 1(b). Structural relaxation resulted in a lattice constant of 3.964 Å.

Phonon dispersion curves calculated along high-symmetry lines Γ - X - M - Γ - R in the Brillouin zone, and partial phonon density of states for each element, are shown in Fig. 1(c). The imaginary vibration modes around Γ , M , and R points indicate that cubic LaWN_3 is dynamically unstable. Strongly unstable antiferrodistortive modes at R (20.78*i* THz) and M (4.61*i* THz) points correspond to rotation of WN_6 octahedra, with the instability region in the projected phonon density of states (PDOS) plot almost exclusively associated with N motions. Three transverse optical modes have large imaginary frequencies (3.879*i* THz) at the Γ point, suggesting the possibility of a ferroelectric transition because the eigenvectors of the Γ point modes correspond to a displacement pattern in which N anions move in the opposite direction to the cations. The directions of the displacement modes are indicated by red arrows in Fig. 1(a).

B. Prediction of low-symmetry phases

Both the high instability of the cubic phase and Goldschmidt's rule point to LaWN_3 undergoing one or more structural phase transitions to lower-symmetry structures. By freezing in the unstable modes (i.e., the ferroelectric mode at Γ and antiferrodistortive modes at R and M) singly and in combination, we examined several low-symmetry phases, identifying the $R3c$ phase as having the lowest lattice energy after structure relaxation.

The energy and structural parameters of the low-symmetry phases are reported in Table I, with data of cubic LaWN_3 included for comparison. Based on the calculated lattice energies, the ground-state structure most likely to have $R3c$ symmetry, and other structures should be dynamically unstable at low temperatures. LaWN_3 with orthorhombic $Pnma$ symmetry was also calculated as this is the most commonly observed space group for oxide perovskites²³. In these cases, undercoordination of the A -site cations associated with low tolerance factors leads to octahedral rotations and antipolar A -site displacements which can ultimately sup-

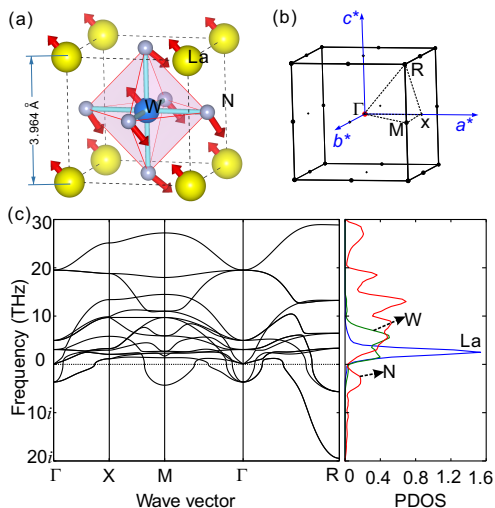


FIG. 1. (Color online) (a) The unit cell of cubic LaWN_3 (space group $Pm\bar{3}m$); (b) the Brillouin zone of a face-centered cubic lattice showing the high-symmetry Γ -X-M- Γ -R path used in phonon calculations. a^* , b^* , and c^* are the primitive reciprocal lattice vectors; and (c) phonon dispersion curves along the high-symmetry k -path and the projected phonon densities of states (PDOSs) normalized to the primitive cell. In the PDOS plot, blue, green, and red curves represent contributions of La, W, and N atoms, respectively.

press the ferroelectricity⁴⁴ The results in Table I show, however, that in the case of LaWN_3 , the $Pnma$ structure is higher in energy than the $R3c$ structure, resulting in the survival of ferroelectricity in LaWN_3 with the $R3c$ form.

Furthermore, in the calculations we also find strongly unstable modes at the Γ point in the case of the $Pnma$ structure (see Fig. S1(a) in Supplementary Material). By freezing in the unstable mode at the Γ point, the structure transforms into a $Pna2_1$ structure. As seen in Table I, the energy of the $Pna2_1$ structure is only 28.12 meV higher than that of $R3c$ structure, indicating $Pna2_1$ LaWN_3 is an alternative metastable phase. As given by the phonon dispersion curves of $Pna2_1$ LaWN_3 (see Fig. S1(b) in Supplementary Material), the imaginary frequencies are disappeared. Since $R3c$ LaWN_3 is the ground-state structure, we focus on the symmetry-related transitions between the three rhombohedral phases to examine the ferroelectric behavior of LaWN_3 in detail. Details of the structural transitions and electronic properties of $Pna2_1$ LaWN_3 are provided as Supplementary Material.

The relative stabilities of the $R\bar{3}c$, $R3m$, and $R3c$ phases were examined by plotting their energies per formula unit (f.u.) as a function of volume per f.u., as shown in Fig. 2(a). The lattice parameter corresponding to the minimum energy for each low-symmetry phase matches the corresponding lattice constant in Table I obtained by freezing in the unstable modes to within about $\pm 0.1\%$. Therefore, both Fig. 2(a) and Table I unambiguously

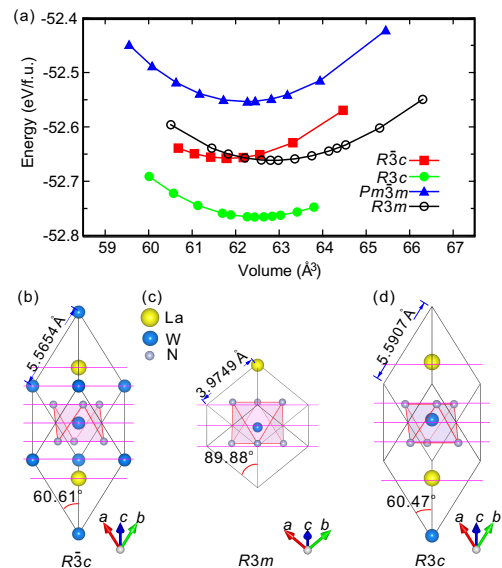


FIG. 2. (Color online) (a) Total energy per formula unit as a function of volume per formula unit for $Pm\bar{3}m$, $R\bar{3}c$, $R3m$, and $R3c$ phases of LaWN_3 . (b) The 10-atom unit cell of the $R\bar{3}c$ structure. (c) The 5-atom unit cell of the $R3m$ structure. (d) The 10-atom unit cell of the ground-state structure ($R3c$). Magenta lines indicate (111) planes. The projection vector for each structure is the [111] direction of the pseudocubic lattice. In the $R\bar{3}c$ structure, W is located at the inversion center, while $R3m$ and $R3c$ structures are non-centrosymmetric, with the W atom displaced from the inversion center in each case.

prove that $R3c$ is the ground-state structure.

The tilting systems in the different phases of LaWN_3 can be described using Glazer's notation.⁴⁵ In rhombohedral nitride perovskites ABN_3 , each BN_6 octahedron is tilted about its triad axis, and this distortion can be described as $a^-a^-a^-$ tilting since adjacent octahedra rotate in opposite directions. In the case of LaWN_3 , both $R3c$ and $R\bar{3}c$ structures belong to this tilting system. The tilting originates from a delicate balance between the rigidity of the WN_6 octahedra and large size difference between La and W ions, and the zone center soft mode. The $R3c$ phase is ferroelectric because of the non-centrosymmetry of its lattice; conversely the $R\bar{3}c$ phase remains non-polar, with B cations located on inversion centers. The $R\bar{3}c$ structure is derived from the $Pm\bar{3}m$ structure purely by an $a^-a^-a^-$ tilting pattern, while the $R3c$ structure is a combination of $a^-a^-a^-$ tilting and displacements of ions along pseudocubic $\langle 111 \rangle$ directions. Unlike the $R3c$ and $R\bar{3}c$ phases, octahedral tilting does not occur in $R3m$ LaWN_3 . However, the space inversion symmetry of the $R3m$ structure is broken, just as it is in the $R3c$ structure, resulting in a net polarization in the z direction.

The calculated rhombohedral structures of the $R\bar{3}c$, $R3m$, and $R3c$ phases are illustrated in Figs. 2(b), (c), and (d), respectively. Although no net dipole moment can be induced in the case of the $R3c$ phase, the non-

TABLE I. Structure parameters, Wyckoff positions, and relative stabilities of different phases of LaWN_3 from DFT-LDA calculations. Each phase is identified by its space group. Stabilities are reported as differences in total energy relative to the $Pm\bar{3}m$ phase. Note that the published version at Phys. Rev. B 95, 014111 (2017) has a typo error in the Wyckoff coordinates of W, which has been fixed here.

Phase	Structure parameters				Atom	Wyckoff site	Coordinates			Energy ΔE (meV/f.u.)
	a (Å)	b (Å)	c (Å)	α (°)			x	y	z	
$Pm\bar{3}m$	3.9635	–	–	90	La	1a	0.0	0.0	0.0	0.0
					W	1b	0.5	0.5	0.5	
					N	3c	0.0	0.5	0.5	
$P4/mbm$	5.5590	–	4.0023	90	La	2d	0.0	0.5	0.0	–53.35
					W	2b	0.0	0.0	0.5	
					N1	4h	0.28917	0.78917	0.5	
					N2	2a	0.0	0.0	0.0	
$I4/mmm$	5.6030	–	7.9231	90	La	4d	0.0	0.5	0.25	–0.51
					W1	2b	0.0	0.0	0.5	
					W2	2a	0.0	0.0	0.0	
					N1	8h	0.24868	0.24868	0.0	
					N2	4e	0.0	0.0	0.25263	
$I4/mcm$	5.6029	–	7.9238	90	La	4a	0.0	0.0	0.25	–0.25
					W	4d	0.0	0.5	0.0	
					N1	8h	0.25171	0.75171	0.0	
					N2	4b	0.0	0.5	0.25	
					N1	8d	0.73057	0.4712	0.2328	
$Pnma$	5.6010	7.9142	5.6386	90	La	4c	–0.01466	0.25	0.49822	–105.93
					W	4a	0.0	0.0	0.0	
					N1	8d	0.73057	0.4712	0.2328	
					N2	4c	0.00373	0.25	–0.05553	
$Pna2_1$	5.5703	5.5992	8.0137	90	La	4a	0.48115	0.49701	0.75	–184.10
					W	4a	0.51666	0.00417	0.00903	
					N1	4a	0.23257	0.23004	0.51592	
					N2	4a	0.71842	0.27548	–0.04178	
					N3	4a	0.50416	–0.05530	0.73893	
$R3m$	3.9749	–	–	89.8841	La	1a	–0.01358	–0.01358	–0.01358	–107.87
					W	1a	0.4863	0.4863	0.4863	
$R3c$	5.5907	–	–	60.4666	La	2a	0.26039	0.26039	0.26039	–212.22
					W	2a	0.01239	0.01239	0.01239	
					N	6b	0.69773	0.79658	0.24290	
$R\bar{3}c$	5.5654	–	–	60.6077	La	2a	0.25	0.25	0.25	–103.94
					W	2b	0.0	0.0	0.0	
					N	6e	0.70144	0.79856	0.25	

centrosymmetry of the $R3c$ and $R3m$ structures makes them candidates for exhibiting ferroelectric behavior. Comparison of the lattice energies in Table I and Fig. 2 shows that the energy of the $R3m$ phase is only 3.9 meV per f.u. lower than that of the $R\bar{3}c$ phase. This small energy difference suggests that the two phases will coexist at low temperatures, not unlike the situation for AgNbO_3 .⁴⁶

The relative stabilities of the three rhombohedral phases can be understood in terms of their vibrational mode frequencies. Figures. 3(a), (b), and (c) show the calculated phonon dispersion curves and projected phonon densities of states for each element for $R\bar{3}c$, $R3m$,

and $R3c$ structures, respectively. The high symmetry path of the first Brillouin zone used in the calculations is shown in Fig. 3(d). The $R3c$ structure does not exhibit any unstable modes, while the $R\bar{3}c$ and $R3m$ structures exhibit strongly unstable modes, confirming that the $R3c$ structure is the ground state. Although the projected PDOSs of the $R3m$ phase are similar to those of the $R\bar{3}c$ phase, the unstable modes are different. Specifically, the imaginary frequencies in the case of the $R3m$ structure occur at points Z and B_1 , corresponding to displacements of N atoms, whereas the centrosymmetric $R\bar{3}c$ phase exhibits an unstable mode at the Γ point that is associated with displacements of all three types of atoms.

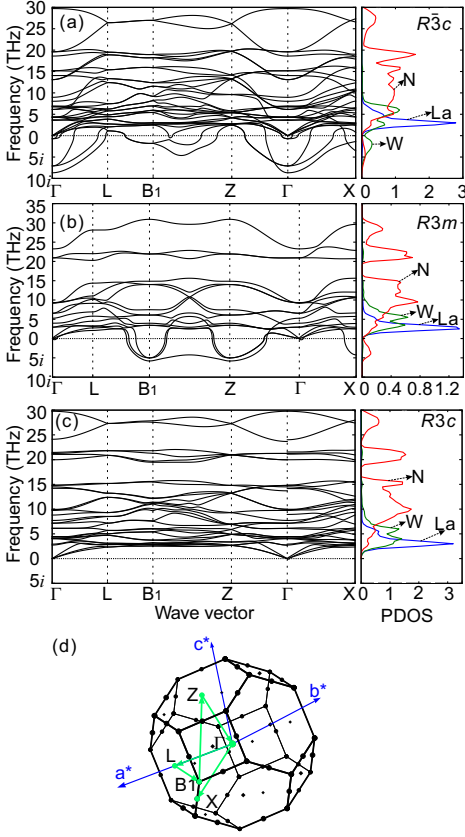


FIG. 3. (Color online) Phonon dispersion curves and projected phonon densities of states (PDOSs) normalized to their respective primitive cells for (a) $R\bar{3}c$, (b) $R3m$, and (c) $R3c$ structures; and (d) the Brillouin zone of the rhombohedral lattice. Blue, green, and red curves in the PDOS plots represent the contributions of La, W, and N atoms, respectively. In (d), the dispersion path (green) passes through special high-symmetry points Γ , L , B_1 , Z , and X . Reciprocal lattice vectors are shown as blue arrows.

$R\bar{3}c$ LaWN_3 has not yet been synthesized, so to assess its chemical stability we calculated the formation enthalpy relative to component phases LaN and WN_2 , whose structures were taken from Ref. 47 and Ref. 48 respectively, according to $\Delta H^f(\text{LaWN}_3) = E(\text{LaWN}_3) - E(\text{LaN}) - E(\text{WN}_2)$, where $E(\text{LaWN}_3)$, $E(\text{LaN})$, and $E(\text{WN}_2)$ are the total energies per f.u. of LaWN_3 , LaN , and WN_2 , respectively. The calculated formation enthalpy of -11.617 eV per f.u. suggests that it should be possible to synthesize LaWN_3 in its $R\bar{3}c$ form.

C. Structural phase transitions

The structural phase transition pathways and mechanisms between the three rhombohedral phases were also investigated using first-principles calculations.

Two possible transition sequences with increasing temperature from the rhombohedral phases to the $Pm\bar{3}m$

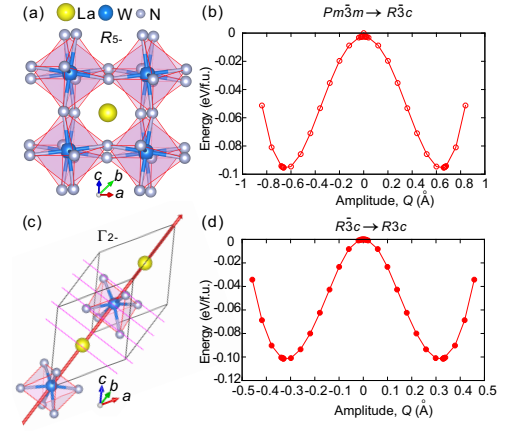


FIG. 4. (Color online) (a) Schematic of the reference structure with only the R_{5-} mode frozen. (b) Energy-amplitude curve for the $Pm\bar{3}m \rightarrow R\bar{3}c$ transition, with energies taken relative to that of the $Pm\bar{3}m$ structure. (c) Schematic representation of the reference structure with Γ_{2-} mode frozen. (d) Energy-amplitude curve for the $R\bar{3}c \rightarrow R3c$ transition, with energies relative to that of the $R\bar{3}c$ structure.

phase were identified from the symmetry relations between the different phases, viz. from the polar $R\bar{3}c$ phase with $a^-a^-a^-$ tilting to the $Pm\bar{3}m$ phase via either the $R\bar{3}c$ or $R3m$ structure. Similarly, upon cooling, the phase transition sequence could be either $Pm\bar{3}m \rightarrow R\bar{3}c \rightarrow R3c$ or $Pm\bar{3}m \rightarrow R3m \rightarrow R3c$. To examine the transition mechanisms in more detail, we calculated the total energy of each phase as a function of the mode amplitude for each of the possible pathways. Here the amplitude Q of a specified mode is defined as $Q = \sqrt{\sum_i \zeta_{i\alpha}^2}$, where ζ_i denotes the displacement of atom i in the direction α from its equilibrium position in the parent structure.

Pathway $Pm\bar{3}m \rightarrow R\bar{3}c \rightarrow R3c$. The transition pathway $Pm\bar{3}m \rightarrow R\bar{3}c$ is associated with the $a^-a^-a^-$ tilting mode with irreducible representation R_{5-} . The tilting mode caused by the rotation of a WN_6 octahedron is illustrated in Fig. 4(a). The amplitude of the distortion is around 0.67 Å. Figure 4(b) shows the associated energy-amplitude curve. The energy to stabilize the WN_6 octahedron is about 95.36 meV per f.u., indicating that the transition from the $R\bar{3}c$ phase to the cubic $Pm\bar{3}m$ phase occurs at a temperature of 1106 K. The transition from $R\bar{3}c$ to $R3c$ is related to the irreducible representation Γ_{2-} with amplitude 0.33 Å. The Γ_{2-} mode involves displacement of W and La atoms in the pseudocubic $[111]$ direction and bending of N-W-N bonds, as illustrated in Fig. 4(c). The double-well shape of the energy-amplitude curve in Fig. (d) indicates the $R\bar{3}c \rightarrow R3c$ ferroelectric transition involves spontaneous symmetry breaking. The energy associated with the Γ_{2-} mode is about 101.4 meV per f.u., corresponding to a temperature increase of 1177 K.

Pathway $Pm\bar{3}m \rightarrow R3m \rightarrow R3c$. The symmetry-

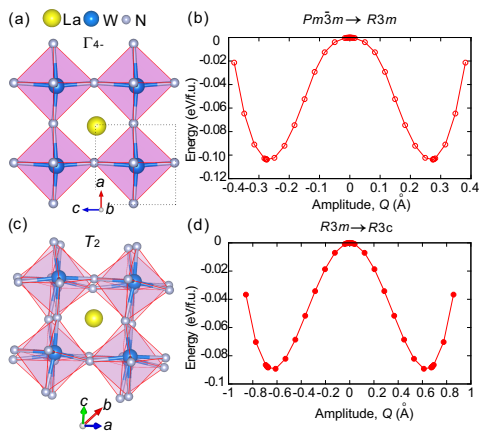


FIG. 5. (Color online) (a) Schematic of the reference structure with frozen symmetry mode Γ_{4-} . (b) Energy-amplitude curve for the $Pm\bar{3}m \rightarrow R3m$ transition, with energies relative to that of the $Pm\bar{3}m$ structure. (c) Schematic of the reference structure with frozen T_2 mode. (d) Energy-amplitude curve for the $R3m \rightarrow R3c$ transition, with energies relative to that of the $R3m$ structure.

adapted modes associated with the $Pm\bar{3}m \rightarrow R3m \rightarrow R3c$ transition are shown in Fig. 5. A four-dimensional Γ_{4-} distortion with an amplitude of 0.28 Å results in a phase transition from the $Pm\bar{3}m$ structure to $R3m$ structure. The structure with the frozen Γ_{4-} mode is shown in Fig. 5(a). This Γ_{4-} mode is contributed by La- T_{1u} , W- T_{1u} , N- A_{2u} , and N- E_u . In the $R3m$ phase, no octahedral tilting occurs, and the inversion center vanishes on account of displacements of La, W, and N atoms along the pseudocubic [111] direction. The energy-amplitude curve in Fig. 5(b) indicates the phase transition from $R3m$ to $Pm\bar{3}m$ requires an energy of 103.75 meV per f.u. Figures 5(c) and (d) show that the $R3c$ structure is stabilized by a T_2 distortion with a large amplitude of 0.68 Å, resulting in an energy decrease of 89.24 meV per f.u. relative to $R3m$. The energy-amplitude curves show that the transition $R3m \rightarrow R3c$ is more energetically favorable than $R\bar{3}c \rightarrow R3c$, consistent with the results in Fig. 2

D. Dielectric and electronic properties

The suitability of a ferroelectric for a particular application depends as much on its electronic properties as its ferroelectric behavior. Using the Berry phase method³⁸, we calculated the ground-state $R3c$ phase of LaWN_3 to have a spontaneous polarization of around $61 \mu\text{C}/\text{cm}^2$. This polarization was calculated relative to an $R\bar{3}c$ structure with the same lattice constants as the polar $R3c$ phase. The $R\bar{3}c$ reference phase was found to be metallic (no band gap), however, so we manually chose suitable switching paths to compute the allowed value of polarization, in the same manner as used by Neaton *et al.* in their study of $R3c$ BiFeO_3 .⁴⁹ Recently Sarmiento-Pérez *et al.*⁵⁰

and Körbel *et al.*²⁷ reported polarization values of 66 and $73 \mu\text{C}/\text{cm}^2$, respectively, for LaWN_3 , which are slightly larger than our value. This discrepancy can be attributed to the different lattice parameters used, since our calculated lattice energy and volume for the $R3c$ phase are 103.48 meV/f.u. and $3.315 \text{ \AA}^3/\text{f.u.}$ smaller, respectively, than that of the structure used by Rafael *et al.*⁵⁰ Also, Körbel *et al.* did not consider rotation of the WN_6 octahedra in their model,²⁷ which results in overestimation of the polarization.

Figures 6(a) and (b) show the total and partial electronic densities of states of $R3c$ LaWN_3 calculated using HSE and LDA functionals, respectively. The corresponding band gaps are 1.72 and 0.81 eV. The HSE hybrid functional typically provides a more accurate estimate of the band gap in semiconductors,⁵¹ but apart from the difference in gap width, the main features of the density of states according to the two methods are almost the same. This justifies our use of the computationally less-expensive LDA functional in calculations of phase stability and ferroelectric transitions.

Figures 6(c), (d) and (e) show the partial densities of states from the LDA calculations of La, W, and N atoms, respectively, split into their s , p , and d component orbitals. The densities of states of La and W either side of the band gap mostly comprise their respective $5d$ and $5p$ states, and those of N are dominated by the $2p$ states. The partial densities of states show La- $5d$, W- $5d$, W- $5p$, and N- $2p$ states undergo significant hybridization. Specifically, the energy separation of these electronic states determines the band gap. The strong cross-gap hybridization between N- $2p$ and unoccupied W- $5d$ states is essential for the onset of the ferroelectric instability, details of which are provided as Supplementary Material. In addition, the small contribution of La- $6s$ states to the bonding suggests that LaWN_3 is different to bismuth-based ferroelectric materials such as BiFeO_3 and BiMnO_3 , in which the ferroelectric instability is caused by the stereochemical activity of the lone-pair electrons of the A-site Bi cations, which do not participate in chemical bonding.^{52,53}

The electronic structure and bonding character of $R3c$ LaWN_3 can be appraised more quantitatively from plots of its electron localization function (ELF) shown in Fig. 7(a). The ELF provides an estimate of the probability of finding an electron at a given location.⁵⁴ A value close to one means there is a high probability of an electron being found at that position, while a value of zero means electrons are fully delocalized or no electron is at that location; an ELF close to one-half corresponds to an electron-gas-like pair distribution. In Fig. 7(a), electron-gas-like regions (red) exist around La and N atoms. The charge distribution around La is also very uniform. This indicates that there are no localized lobe-shaped charge distributions (lone-pair electrons), in contrast to BiMnO_3 , whose lone pairs are readily apparent in ELF plots.⁵² In the case of LaWN_3 , electrons are strongly localized around N, and the maximum value of the ELF between

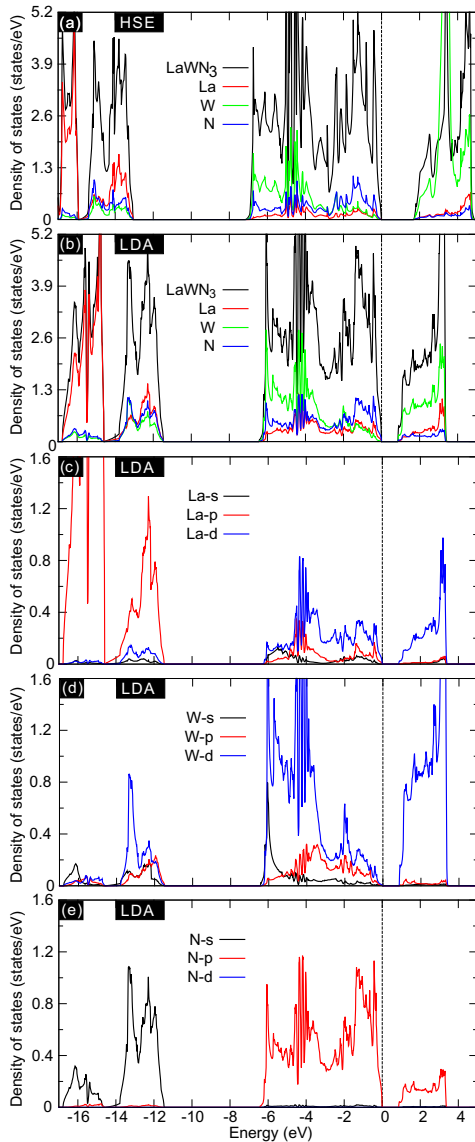


FIG. 6. (Color online) Total and partial electronic densities of states of ferroelectric $R3c$ phase using the (a) HSE functional, and (b) LDA functional. The total densities of states are normalized to one formula unit. (c), (d), and (e) show the densities of states projected onto orbitals of La, W, and N atoms, respectively. The Fermi level is at 0 eV.

La and N is less than 0.2, suggesting that the La-N bond is mostly ionic. In contrast, electrons around W appear almost fully delocalized, so ELF values near W atoms are much smaller than near La atoms, indicating a higher covalency of the W-N bond. Based on the charge density difference maps in Fig. 7(b), more electrons are transferred from W to N than from La to N. Moreover, in the 2D slice in the right-hand panel, some electrons are localized between W and N atoms, which confirms W and N bond by sharing electron pairs.

Quantitative charge analyses were also carried out to evaluate the nature of the bonding, i.e., the amount of

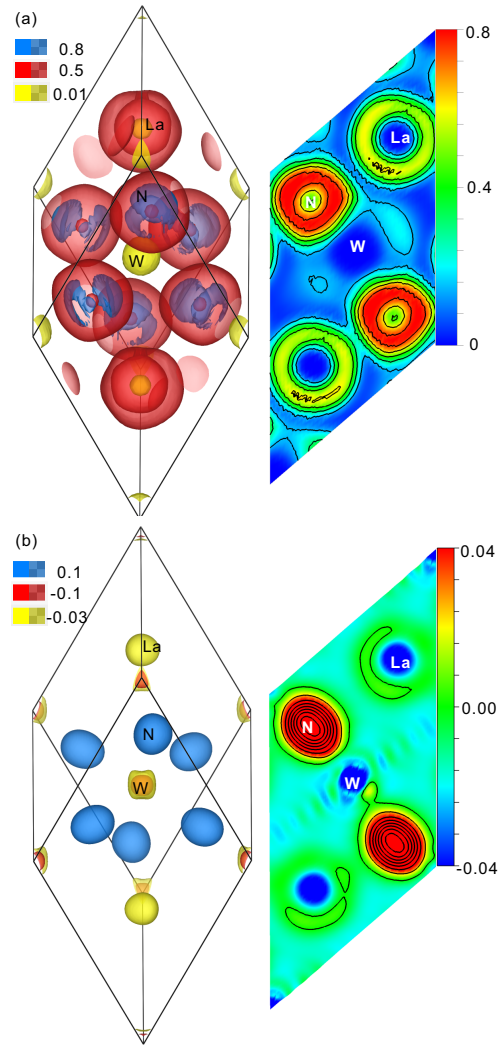


FIG. 7. (Color online) (a) Maps of the electron localization function (ELF) in a unit cell of $R3c$ LaWN_3 : left, 3D isosurface plot; right, 2D slice through the $(1\bar{1}0)$ plane. Isosurface values are set at 0.8 (blue), 0.5 (red), and 0.01 (yellow). (b) Charge density difference maps in a unit cell of $R3c$ LaWN_3 : left, 3D isosurface plot; right: slice through the $(1\bar{1}0)$ plane. Isosurface values are set at 0.1 (blue), -0.1 (red) and -0.03 (yellow). Charge density differences were obtained by subtracting superposed atomic densities from the charge density of the $R3c$ LaWN_3 crystal.

charge transfer between atoms, in $R3c$ LaWN_3 . Born effective charges Z^* were obtained using the density functional perturbation theory method. The diagonal entries in the tensor matrices for La, W, and N in Table II are all much larger than their nominal ionic charges, consistent with LaWN_3 being strongly polarizable; in particular, the much larger Born effective charge of W suggests that W-N bonds are more covalent than La-N bonds. Similarly, Bader (static) charges calculated for La, W, and N of +1.86e, +2.15e, and -1.34e, respectively, are smaller than their nominal charges by 38%, 64%, and 55%, respectively, which also points to greater covalency in the

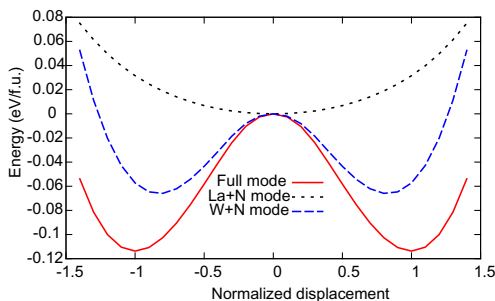


FIG. 8. (Color online) Energy as a function of normalized displacement for full mode (red solid curve), La+N partial mode (black dot curve), and W+N partial mode (blue dash curve) in LaWN₃. The amplitude of the ion displacements along $\langle 111 \rangle$ directions are normalized, i.e., 1 corresponds to the ferroelectric state with $R3c$ symmetry, and 0 corresponds to the paraelectric state with $R\bar{3}c$ symmetry.

W-N bonds, since the smaller the magnitude of the Bader charge, the less ionized the atom is. The charge analyses thus confirm the trends observed from ELF analysis and charge density difference maps.

To probe the microscopic mechanism of the ferroelectric phase transition in LaWN₃ further, we calculated the potential energy profile during polarization switching. A combination of soft modes at the Γ point (i.e., Γ_{2-} and Γ_{1+} modes) was used as the full mode to which the displacements of all atoms were compared. We also examined the La+N mode, in which atomic displacements of W are neglected, to study the partial contribution of La ions; similarly the W+N mode was probed to determine the contribution of W ions. The obtained curves are shown in Fig. 8. The results reveal that the double-well potential vanishes in the case of the La+N mode, indicating that the La atom is dynamically unstable on its intermediate position. A double-well potential appears in the case of the W+N mode, although the depth of the wells is slightly shallower than those of the full mode. This indicates that ferroelectricity in LaWN₃ mostly arises from motion of the W ions, and not the La ion displacements. This is unusual because ferroelectricity in LiNbO₃-type materials is associated with A -site displacement for most oxide perovskites with tolerance factors less than 1.^{17,28,29,55}

In the $R3c$ form of LaWN₃ ($t = 0.969$), although the A -site cation is displaced from its centrosymmetric site, this does not give rise to its ferroelectricity. The microscopic origin of ferroelectricity in LaWN₃ thus appears to be similar to that in LiNbO₃. In LiNbO₃, the ferroelectric instability is driven by the hybridization of Nb- $4d$ and O- $2p$ states, which causes O anions to be displaced toward the Nb ions; displacements of O anions result in displacements of Li ions from their centrosymmetric positions.²¹ Similarly, the driving mechanism of ferroelectricity in LaWN₃ is the hybridization of W- $5d$ and N- $2p$

states (see Figs. S4 and S5 in Supplementary Material), which leads to relative displacements of W cations and N anions, with the displacements of N cations pushing La ions off their centrosymmetric positions. A -site cations thus play a passive role in the ferroelectric transition in LaWN₃, as shown in Fig. 8, only displacements of W ions drive the ferroelectric instability of LaWN₃, in contrast, both Nb and Li displacements contribute to the ferroelectric instability of LiNbO₃.²⁹

IV. SUMMARY

First-principles calculations of perovskite-type ferroelectric nitride LaWN₃ within the framework of density functional theory have enabled us to determine the key structural distortions controlling the ferroelectric phase transition. The $Pm\bar{3}m$ (cubic) form is unstable at 0 K and will spontaneously transform to the ground-state $R3c$ phase. By studying the relationship between structure stability and symmetry-adapted distortions, two transition pathways associated with ground-state $R3c$ LaWN₃, viz. $Pm\bar{3}m \rightarrow R\bar{3}c \rightarrow R3c$ and $Pm\bar{3}m \rightarrow R3m \rightarrow R3c$, have been elucidated. The strong hybridization of W- $5d$ and N- $2p$ states produces a band gap of 1.72 eV according to hybrid functional calculations. The strong interaction results in displacements of W and N ions, indirectly leading to displacement of La ions through their interaction with N ions. All these displacements are involved in optimizing the coordination environments of A -site and B -site cations, but only the displacements of B -site W cations along the pseudocubic $[111]$ direction drive the ferroelectric instability in $R3c$ LaWN₃. The large spontaneous polarization of about 61 $\mu\text{C}/\text{cm}^2$ and exothermic formation enthalpy of -11.617 eV/f.u. calculated for LaWN₃ indicate it should be a good ferroelectric material synthesizable under appropriate conditions. Experiments to determine the optimum method and conditions for synthesizing LaWN₃ and to confirm its ferroelectric behavior are currently under way.

ACKNOWLEDGMENTS

The computational sources have been provided by the computing center of ECNU, Nanostructures Research Laboratory of JFCC, and Chinese Tianhe-1A system of National Supercomputer Center. The authors are grateful to N. Otani, A. Konishi, K. Shitara, and Hongjian Zhao for valuable discussions. The work at ECNU was supported by the National Basic Research Program of China (Grant No. 2014CB921104, 2013CB922301) and NSFC (Grant No. 51572085). Y.-W.F. thanks the Doctoral Mobility Scholarship at ECNU for funding his stay at JFCC. R.H. was partially supported by Natural Science Foundation of Shanghai (Grant No. 16ZR1409500)

TABLE II. Eigenvalues of calculated Born effective charge tensors Z^* for La, W, and N in $R3c$ LaWN₃.

Atom	Coordinates			Eigenvalues								
	x	y	z	Z_{xx}^*	Z_{yy}^*	Z_{zz}^*	Z_{xy}^*	Z_{xz}^*	Z_{yx}^*	Z_{zx}^*	Z_{zy}^*	
La	0.260	0.260	0.260	4.517	4.517	4.107	0.436	0	-0.437	0	0	0
La	0.760	0.760	0.760	4.517	4.517	4.107	-0.436	0	0.437	0	0	0
W	0.012	0.012	0.012	10.571	10.571	6.844	-0.775	0	0.774	0	0	0
W	0.512	0.512	0.512	10.571	10.571	6.844	0.775	0	-0.774	0	0	0
N	0.698	0.797	0.243	-3.204	-6.856	-3.650	0.270	0.139	0.566	-1.882	0.255	-1.753
N	0.243	0.698	0.797	-5.581	-4.478	-3.651	-1.939	1.561	-1.642	1.061	1.391	1.098
N	0.797	0.243	0.698	-6.304	-3.754	-3.651	1.224	-1.670	1.521	0.821	-1.646	0.655
N	0.297	0.198	0.743	-3.203	-6.856	-3.651	-0.270	-0.139	-0.566	-1.882	-0.255	-1.753
N	0.743	0.297	0.198	-6.304	-3.754	-3.651	-1.225	1.670	-1.521	0.821	1.646	0.656
N	0.198	0.743	0.297	-5.581	-4.478	-3.651	1.939	-1.561	1.642	1.062	-1.391	1.098

- * cgduan@clpm.ecnu.edu.cn, † moriwake@jfcc.or.jp, ‡ fyuewen@gmail.com
- ¹ D. Lee, H. Lu, Y. Gu, S.-Y. Choi, S.-D. Li, S. Ryu, T. R. Paudel, K. Song, E. Mikheev, S. Lee, S. Stemmer, D. A. Tenne, S. H. Oh, E. Y. Tsybal, X. Wu, L.-Q. Chen, A. Gruverman, and C. B. Eom, *Science* **349**, 1314 (2015).
 - ² Y. L. Tang, Y. L. Zhu, X. L. Ma, A. Y. Borisevich, A. N. Morozovska, E. A. Eliseev, W. Y. Wang, Y. J. Wang, Y. B. Xu, Z. D. Zhang, and S. J. Pennycook, *Science* **348**, 547 (2015).
 - ³ N. C. Bristowe, J. Varignon, D. Fontaine, E. Bousquet, and P. Ghosez, *Nat. Commun.* **6**, 6677 (2015).
 - ⁴ H. Wang, J. Wen, D. J. Miller, Q. Zhou, M. Chen, H. N. Lee, K. M. Rabe, and X. Wu, *Phy. Rev. X* **6**, 011027 (2016).
 - ⁵ H.-J. Liu, J.-C. Lin, Y.-W. Fang, J.-C. Wang, B.-C. Huang, X. Gao, R. Huang, P. R. Dean, P. D. Hatton, Y.-Y. Chin, H.-J. Lin, C.-T. Chen, Y. Ikuhara, Y.-P. Chiu, C.-S. Chang, C.-G. Duan, Q. He, and Y.-H. Chu, *Adv. Mater.* **28**, 9142 (2016).
 - ⁶ V. Garcia and M. Bibes, *Nat. Commun.* **5**, 4289 (2014).
 - ⁷ D. Lee, S. M. Yang, T. H. Kim, B. C. Jeon, Y. S. Kim, J.-G. Yoon, H. N. Lee, S. H. Baek, C. B. Eom, and T. W. Noh, *Adv. Mater.* **24**, 402 (2012).
 - ⁸ K. T. Butler, J. M. Frost, and A. Walsh, *Energy Environ. Sci.* **8**, 838 (2015).
 - ⁹ R. Nechache, C. Harnagea, S. Li, L. Cardenas, W. Huang, J. Chakrabartty, and F. Rosei, *Nat. Photon.* **9**, 61 (2015).
 - ¹⁰ T. P.-C. Juan, C.-L. Lin, W.-C. Shih, C.-C. Yang, J. Y.-M. Lee, D.-C. Shye, and J.-H. Lu, *J. Appl. Phys.* **105**, 061625 (2009).
 - ¹¹ P. K. Panda, *J. Mater. Sci.* **44**, 5049 (2009).
 - ¹² J. C. Agar, S. Pandya, R. Xu, A. K. Yadav, Z. Liu, T. Angsten, S. Saremi, M. Asta, R. Ramesh, and L. W. Martin, *MRS Commun.* **FirstView**, 1 (2016).
 - ¹³ M. Ye and D. Vanderbilt, *Phys. Rev. B* **93**, 134303 (2016).
 - ¹⁴ C. Xie, A. R. Oganov, D. Dong, N. Liu, D. Li, and T. T. Debela, *Sci. Rep.* **5**, 16769 (2015).
 - ¹⁵ R. Armiento, B. Kozinsky, M. Fornari, and G. Ceder, *Phys. Rev. B* **84**, 014103 (2011).
 - ¹⁶ A. A. Belik, W. Yi, Y. Kumagai, Y. Katsuya, M. Tanaka, and F. Oba, *Inorg. Chem.* **55**, 1940 (2016).
 - ¹⁷ P. S. Wang, W. Ren, L. Bellaiche, and H. J. Xiang, *Phys. Rev. Lett.* **114**, 147204 (2015).
 - ¹⁸ X. F. Hao, A. Stroppa, S. Picozzi, A. Filippetti, and C. Franchini, *Phys. Rev. B* **86**, 014116 (2012).
 - ¹⁹ J. Zhang, K. L. Yao, Z. L. Liu, G. Y. Gao, Z. Y. Sun, and S. W. Fan, *Phys. Chem. Chem. Phys.* **12**, 9197 (2010).
 - ²⁰ C.-G. Duan, W. N. Mei, J. Liu, W.-G. Yin, J. R. Hardy, R. W. Smith, M. J. Mehl, and L. L. Boyer, *Phys. Rev. B* **69**, 033102 (2004).
 - ²¹ I. Inbar and R. E. Cohen, *Phy. Rev. B* **53**, 1193 (1996).
 - ²² C. J. Fennie, *Phys. Rev. Lett.* **100**, 167203 (2008).
 - ²³ N. A. Benedek and C. J. Fennie, *J. Phy. Chem. C* **117**, 13339 (2013).
 - ²⁴ T. Varga, A. Kumar, E. Vlahos, S. Denev, M. Park, S. Hong, T. Sanehira, Y. Wang, C. J. Fennie, S. K. Streiffer, X. Ke, P. Schiffer, V. Gopalan, and J. F. Mitchell, *Phys. Rev. Lett.* **103**, 047601 (2009).
 - ²⁵ E. H. Smith, N. A. Benedek, and C. J. Fennie, *Inorg. Chem.* **54**, 8536 (2015).
 - ²⁶ R. Sarmiento-Pérez, T. F. T. Cerqueira, S. Körbel, S. Botti, and M. A. L. Marques, *Chem. Mater.* **27**, 5957 (2015).
 - ²⁷ S. Körbel, M. A. L. Marques, and S. Botti, *J. Mater. Chem. C* **4**, 3157 (2016).
 - ²⁸ Y. Inaguma, M. Yoshida, and T. Katsumata, *J. Am. Chem. Soc.* **130**, 6704 (2008).
 - ²⁹ H. J. Xiang, *Phys. Rev. B* **90**, 094108 (2014).
 - ³⁰ H. M. Liu, Y. P. Du, Y. L. Xie, J.-M. Liu, C.-G. Duan, and X. Wan, *Phys. Rev. B* **91**, 064104 (2015).
 - ³¹ G. Kresse and J. Furthmüller, *Comp. Mater. Sci.* **6**, 15 (1996).
 - ³² G. Kresse and J. Furthmüller, *Phys. Rev. B* **54**, 11169 (1996).
 - ³³ P. E. Blöchl, *Phys. Rev. B* **50**, 17953 (1994).
 - ³⁴ H. J. Monkhorst and J. D. Pack, *Phys. Rev. B* **13**, 5188 (1976).
 - ³⁵ X. Gonze and C. Lee, *Phys. Rev. B* **55**, 10355 (1997).
 - ³⁶ A. Togo and I. Tanaka, *Scripta. Mater.* **108**, 1 (2015).
 - ³⁷ Y. Wang, J. J. Wang, W. Y. Wang, Z. G. Mei, S. L. Shang, L. Q. Chen, and Z. K. Liu, *J. Phys.: Condens. Matter* **22**, 202201 (2010).

- ³⁸ R. D. King-Smith and D. Vanderbilt, *Phys. Rev. B* **47**, 1651 (1993).
- ³⁹ X. Wan, J. Zhou, and J. Dong, *Europhys. Lett.* **92**, 57007 (2010).
- ² Y.-W. Fang, H.-C. Ding, W.-Y. Tong, W.-J. Zhu, X. Shen, S.-J. Gong, X.-G. Wan, and C.-G. Duan, *Sci. Bull.* **60**, 156 (2015).
- ⁴¹ J. Heyd, G. E. Scuseria, and M. Ernzerhof, *J. Chem. Phys.* **118**, 8207 (2003).
- ⁴² M. R. Filip, G. E. Eperon, H. J. Snaith, and F. Giustino, *Nat. Commun.* **5** (2014).
- ⁴³ J. W. Bennett, I. Grinberg, and A. M. Rappe, *Phys. Rev. B* **73**, 180102 (2006).
- ⁴⁴ N. A. Benedek, A. T. Mulder, and C. J. Fennie, *J. Solid State Chem.* **195**, 11 (2012).
- ⁴⁵ A. M. Glazer, *Acta Crystallogr., Sect. B* **28**, 3384 (1972).
- ⁴⁶ H. Moriwake, A. Konishi, T. Ogawa, C. A. J. Fisher, A. Kuwabara, and D. Fu, *J. Appl. Phys.* **119**, 064102 (2016).
- ⁴⁷ V. I. Khitrova, *Sov. Phys. Crystallogr.* **6**, 439 (1961).
- ⁴⁸ G. L. Olcese, *J. Phys. F: Met. Phys.* **9**, 569 (1979).
- ⁴⁹ J. B. Neaton, C. Ederer, U. V. Waghmare, N. A. Spaldin, and K. M. Rabe, *Phys. Rev. B* **71**, 014113 (2005).
- ⁵⁰ R. Sarmiento-Pérez, T. F. T. Cerqueira, S. Körbel, S. Botti, and M. A. L. Marques, *Chem. Mater.* **27**, 5957 (2015).
- ⁵¹ J. Heyd, J. E. Peralta, G. E. Scuseria, and R. L. Martin, *J. Chem. Phys.* **123**, 174101 (2005).
- ⁵² R. Seshadri and N. A. Hill, *Chem. Mater.* **13**, 2892 (2001).
- ⁵³ D. Khomskii, *J. Magn. Magn. Mater.* **306**, 1 (2006).
- ⁵⁴ A. D. Becke and K. E. Edgecombe, *J. Chem. Phys.* **92**, 5397 (1990).
- ⁵⁵ R. Takahashi, I. Ohkubo, K. Yamauchi, M. Kitamura, Y. Sakurai, M. Oshima, T. Oguchi, Y. Cho, and M. Lippmaa, *Phys. Rev. B* **91**, 134107 (2015).

Appendix A: I. Structural stability of $Pnma$ and $Pna2_1$ structures

Calculated phonon dispersion curves and projected phonon densities of states (PDOS) of $Pnma$ LaWN_3 are shown in Fig. S1(a). Strongly unstable modes occur at the Γ point. Freezing in these unstable modes leads to the $Pna2_1$ phase. Fig. S1(b) shows the phonon dispersion curves and PDOS of $Pna2_1$ LaWN_3 . In this case, the unstable modes have almost disappeared at the Γ point, implying it is more dynamically stable than the $Pnma$ phase.

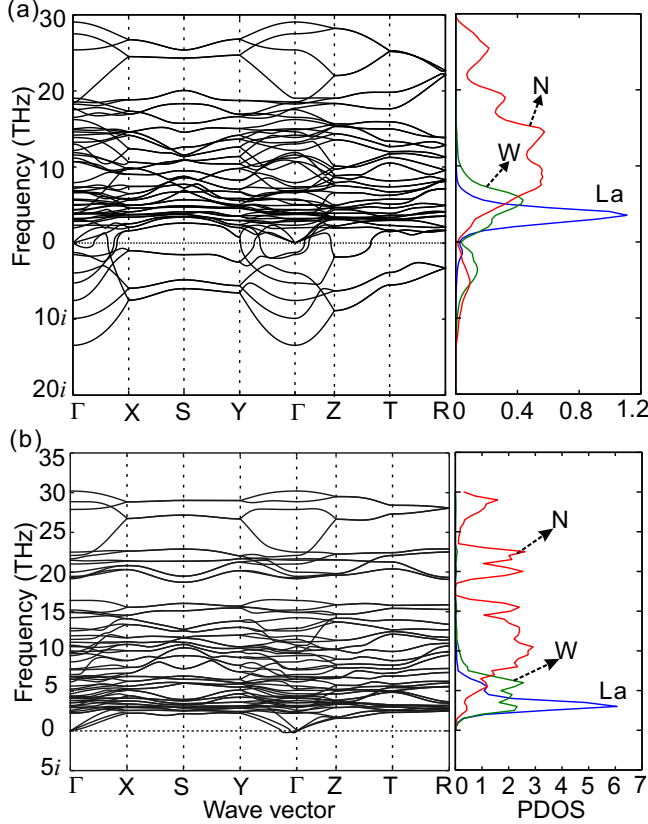


Figure S1. (Color online) Phonon dispersion curves and projected phonon densities of states (PDOSs) of (a) $Pnma$ and (b) $Pna2_1$ LaWN_3 . In the PDOS plots, blue, green, and red curves represent contributions of La, W, and N atoms, respectively.

Appendix B: II. Structural phase transitions associated with $Pna2_1$ symmetry

The pathway $Pm\bar{3}m \rightarrow Pnma \rightarrow Pna2_1$ was investigated by calculating the energy per formula unit (f.u.) as a function of mode amplitude. The transition from the $Pm\bar{3}m$ phase to $Pnma$ phase involves a combination of R_{5-} and Γ_{2+} distortion modes; hence the $Pm\bar{3}m \rightarrow Pnma$ transition is a combination

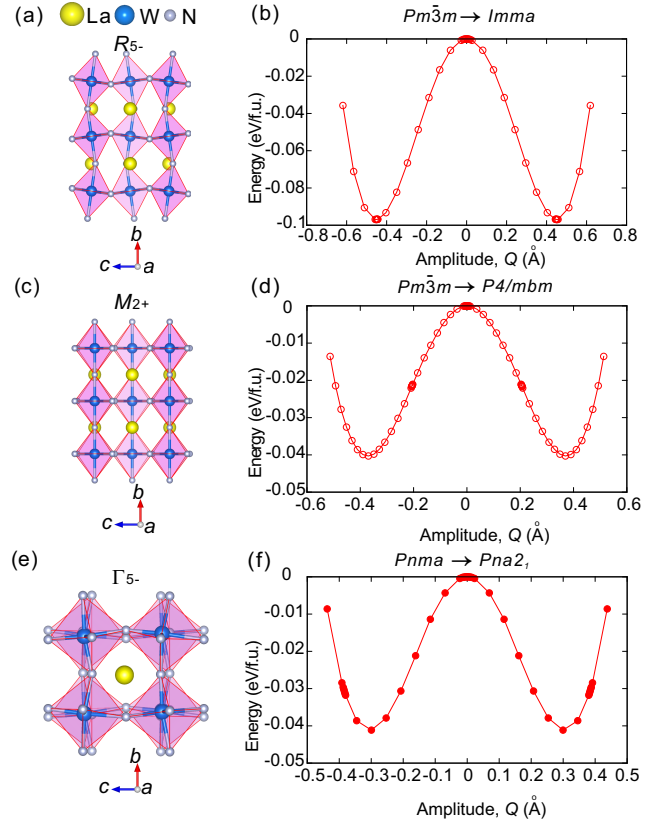


Figure S2. (Color online) Schematics of (a) the $Imma$ reference structure with only the R_{5-} mode frozen, (b) the $P4/mbm$ reference structure with only the M_{2+} mode frozen, and (c) the $Pna2_1$ reference structure with the Γ_{5-} mode frozen. (d), (e) and (f) show the energy-amplitude curves for $Pm\bar{3}m \rightarrow Imma$, $Pm\bar{3}m \rightarrow P4/mbm$, and $Pnma \rightarrow Pna2_1$ transitions, respectively. Energies in (d) and (e) are relative to that of the $Pm\bar{3}m$ structure, while those in (e) the $Pnma$ structure.

of $Pm\bar{3}m \rightarrow Imma$ and $Pm\bar{3}m \rightarrow P4/mbm$ transitions. The $Imma$, $P4/mbm$, and $Pna2_1$ reference structures are shown in Figs. S2(a), (b), and (c), respectively. Energy-amplitude curves for $Pm\bar{3}m \rightarrow Imma$, $Pm\bar{3}m \rightarrow P4/mbm$, and $Pnma \rightarrow Pna2_1$ transitions are shown in Figs. S2(d), (e), and (f), respectively. For the transition $Pnma \rightarrow Pna2_1$, the symmetry-adapted mode is mainly composed of the Γ_{5-} mode.

Appendix C: III. Electronic properties and ferroelectric polarization of the $Pna2_1$ phase

The band gap of $Pna2_1$ LaWN_3 obtained from HSE hybrid calculations is about 1.25 eV. The ferroelectric polarization was calculated to be about $20 \mu\text{C}/\text{cm}^2$.

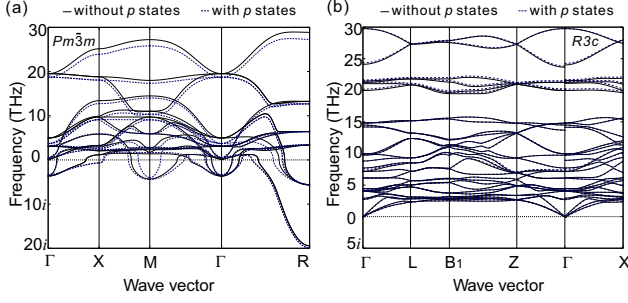


Figure S3. (Color online) Phonon dispersion curves of (a) $Pm\bar{3}m$ and (b) ferroelectric $R3c$ LaWN_3 . Phonon dispersion curves calculated with (without) semi-core W p states are plotted as black solid (blue dashed) lines.

Appendix D: IV. Effect of semi-core W p states on ferroelectric instability

Figure S3 compares the phonon dispersion curves of (a) $Pm\bar{3}m$ and (b) $R3c$ LaWN_3 . For $Pm\bar{3}m$ LaWN_3 , pseudopotentials with and without semi-core W p states included both reproduce the unstable modes at the Γ point. Furthermore, the phonon dispersions along the high-symmetry line ($\Gamma \rightarrow L \rightarrow B_1 \rightarrow Z \rightarrow \Gamma \rightarrow X$) of $R3c$ LaWN_3 are almost identical. These results indicate that semi-core W p states have little influence on the strong ferroelectric instability of LaWN_3 .

Ferroelectric polarization values calculated using pseudopotentials with and without semi-core W p states were also the same ($61 \mu\text{C}/\text{cm}^2$).

Therefore, the pseudopotentials used in our main text are adequate for reproducing the strong ferroelectric instability of LaWN_3 .

Appendix E: V. The influence of hybridization between W - $5d$ and N - $2p$ on the ferroelectric polarization

Using the orbital selective external potential (OSEP) method,^{1,2} we investigated the effects of hybridization of unoccupied W - $5d$ and N - $2p$ orbitals on the ferroelectric polarization of $R3c$ LaWN_3 . This method has previously been implemented and used to study the microscopic mechanism of ferroelectricity in oxide perovskite.²

External fields were applied to N - $2p$ orbitals to modulate the strength of cross-gap hybridization between N - $2p$ and W - $5p$ states. Figure S4 compares the partial densities of states of W - $5d$ and N - $2p$ orbitals calculated by OSEP and LDA methods. The results show that cross-gap hybridization between N - $2p$ and W - $5d$ states is enhanced (decreased) by applying a -1 eV ($+1$ eV) field to N - $2p$ orbitals. The corresponding double-well shaped energy-amplitude curves are shown in Fig. S5. The curves are affected strongly when an electric field is ap-

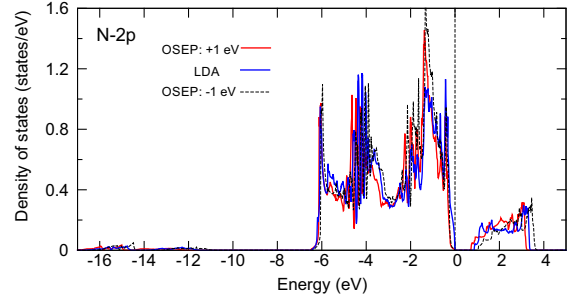
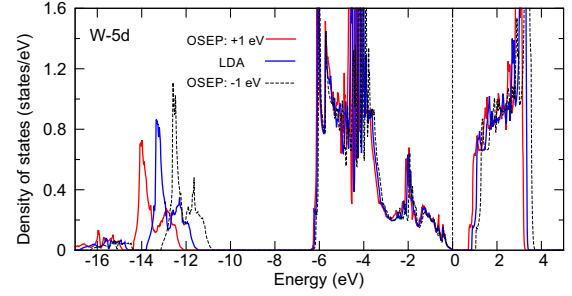


Figure S4. (Color online) Partial densities of states of W - $5d$ and N - $2p$ orbitals calculated by using OSEP and LDA methods. In the OSEP calculations, an external field of ± 1 eV was applied to the N - $2p$ orbitals.

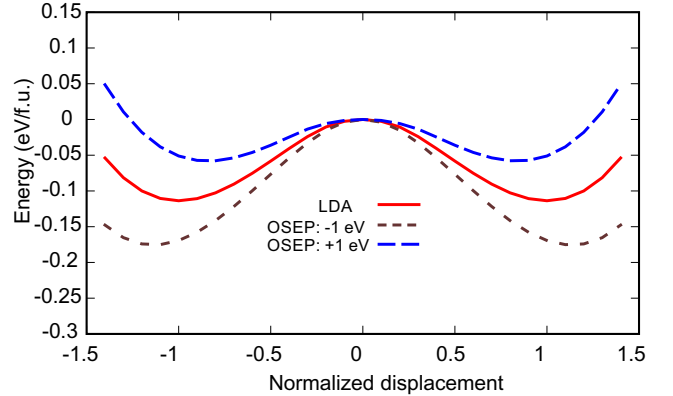


Figure S5. (Color online) Energy as a function of normalized displacement obtained using OSEP and LDA methods. In the case of LDA calculations, a normalized displacement of 1 corresponds to the ferroelectric $R3c$ structure, while 0 displacement corresponds to the paraelectric $R\bar{3}c$ structure.

plied. A $+1$ eV field on N - $2p$ orbitals makes the double-well shallower, while a -1 eV field makes the double-well deeper. In the former case, the calculated ferroelectric polarization is $59.6 \mu\text{C}/\text{cm}^2$ ($< 61 \mu\text{C}/\text{cm}^2$ in LDA), while in the latter case the polarization is $61.4 \mu\text{C}/\text{cm}^2$ ($> 61 \mu\text{C}/\text{cm}^2$ in LDA). These results confirm that the cross-gap hybridization between W - $5d$ and N - $2p$ states is the driving force for ferroelectricity in LaWN_3 .

* cgduan@clpm.ecnu.edu.cn, † moriwake@jfcc.or.jp, ‡
fyuewen@gmail.com

¹ X. G. Wan, J. Zhou, and J. M. Dong, *Europhys. Lett.* **92**,
57007 (2010).

² Y.-W. Fang, H.-C. Ding, W.-Y. Tong, W.-J. Zhu, X. Shen,
S.-J. Gong, X.-G. Wan, and C.-G. Duan, *Sci. Bull.* **60**, 156
(2015).